Understanding the Roles of NiO_x in Enhancing the Photoelectrochemical Performance of $BiVO_4$ Photoanodes for Solar Water Splitting

Mengyuan Zhang,[a] Rajini P. Antony,[a, b] Sing Yang Chiam,[c] Fatwa Firdaus Abdi,*[d] and Lydia Helena Wong*[a]

Abstract: Solar water oxidation is considered as one of the most promising methods to utilize solar energy efficiently, and bismuth vanadate ($BiVO_4$) is a potential photoanode. Catalyst loading on $BiVO_4$ is often used to tackle the limitations of charge recombination and sluggish kinetics. In this study, amorphous nickel oxide (NiO_x) is loaded on $BiVO_4$ by photochemical metal organic deposition method. The resulting NiO_x/Mo:$BiVO_4$ photoanodes demonstrates a 2-fold improvement of photocurrent density of 2.44 mA cm^{-2} at 1.23 V vs. RHE as compared with uncatalyzed samples. After NiO_x modification, both the charge separation and the charge transfer efficiency significantly increase across the entire potential range. It is further elucidated by open circuit photovoltage (OCP), time-resolved microwave conductivity (TRMC) and rapid scan voltammetry (RSV) measurements that NiO_x modification introduces larger band bending and promotes efficient charge transfer on the surface of $BiVO_4$. Our work provides insights into designing excellent $BiVO_4$-catalyst assemblies using a simple surface modification route for efficient solar water oxidation.

Introduction

Photoelectrochemical (PEC) water splitting using semiconductors has been considered a promising solution to overcome the intermittency of solar energy.[1] As one of the promising semiconductor candidates to be used in PEC water splitting, $BiVO_4$ has a suitable band alignment, where the valence band is positive enough for water oxidation while its conduction band is close to the hydrogen evolution potential.[2] The ≈ 2.4 eV bandgap enables monoclinic $BiVO_4$ to absorb up to 11% of the photon flux in solar spectrum,[3] which can theoretically generate a photocurrent of 7.5 mA cm^{-2}.[4] Similar to other metal oxide semiconductors (Fe_2O_3, WO_3, etc.), the photoelectrochemical performance of pristine $BiVO_4$ is hindered by poor charge separation[3, 5] and sluggish charge transfer kinetics.[5-6] To overcome these, various modification methods, such as doping,[1b, 7] catalyst loading,[2a, 8] nanostructuring,[5, 8a, 9] forming heterojunctions or composites,[5, 10] have been widely applied.

Modification by loading earth-abundant catalysts, such as cobalt phosphate (Co-Pi),[3, 5] FeOOH,[2a, 8a] and CoO_x (CoO, Co_2O_3 or Co_3O_4),[8b, 8c, 11] has been utilized to achieve enhanced PEC performance and stability on $BiVO_4$. Typically, these catalysts only affect the surface charge transfer processes, either via increasing catalytic activity or suppressing surface recombination, which has been recently shown to greatly limit the performance of $BiVO_4$.[12] In contrast, nickel oxide (NiO_x) catalysts may potentially provide further functionality; loading NiO_x onto $BiVO_4$ would construct a buried p-n junction, which can facilitate charge separation within $BiVO_4$ photoanode.[8b, 13] This is in addition to the profound catalytic ability and proper band alignment,[14] suppression of surface recombination through passivation,[9] and durable protection against corrosion.[15] However, this expected multifunctionality is still not convincingly shown, since existing NiO_x/$BiVO_4$ systems either normally combine other catalysts to achieve high performance [8b, 16] or utilizes sub-optimal deposition leading to relatively low performance.[9, 13b]

In the present study, we employed a simple, inexpensive but effective photochemical metal organic deposition (PMOD) method to deposit a thin layer of amorphous nickel oxide (NiO_x) on Molybdenum (Mo) gradient-doped $BiVO_4$ (Mo:$BiVO_4$). Our graded Mo:$BiVO_4$ has been investigated previously to enhance the diffusion length and charge separation.[17] Here, NiO_x catalyst modified photoanode offers superior performance than the unmodified one; we show that both bulk and surface recombination are reduced with the deposition of NiO_x as evident from the higher charge injection and charge transfer efficiencies. Through open circuit potential measurements, the enhancement in charge separation was mainly attributed to the enlarged band bending induced by NiO_x layer, which enables efficient carrier transport. Time-resolved microwave conductivity

[a] *M. Zhang, Dr. R. P. Antony, Prof. L. H. Wong*
School of Materials Science and Engineering
Nanyang Technological University
Nanyang Avenue
Singapore 639798 Singapore
E-mail: lydiawong@ntu.edu.sg
[b] *Dr. R. P. Antony*
Chemistry Division, Chemistry Group
Bhabha Atomic Research Center
Mumbai 400085 India
[c] *Dr. S. Y. Chiam*
Institute of Materials Research and Engineering
*A*STAR (Agency for Science, Technology and Research)*
Innovis, 2 Fusionopolis Way
Singapore 138634 Singapore
[d] *Dr. F. F. Abdi*
Institute for Solar Fuels
Helmholtz-Zentrum Berlin für Materialien und Energie GmbH
Hahn-Meitner-Platz 1
Berlin 14109 Germany
E-mail: fatwa.abdi@helmholtz-berlin.de

Supporting information for this article is given via a link at the end of the document.((Please delete this text if not appropriate))

(TRMC) measurements first employed in NiO_x-$BiVO_4$ system as well as rapid scan voltammetry (RSV) measurements also reveal the additional role of NiO_x in aiding efficient charge transfer at the $BiVO_4$ surface. Overall, as a result of these improvements, the AM1.5 photocurrent is enhanced by a factor of ≈ 2 with the deposition of NiO_x on Mo:$BiVO_4$ films.

Results and Discussion

Physical characterizations

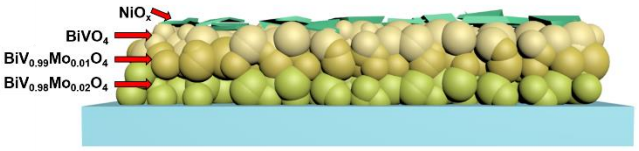

Figure 1. Side-view schematic illustration of NiO_x/Mo:$BiVO_4$ sample.

The schematic illustration of the NiO_x catalyst on $BiVO_4$ is shown in **Figure 1**. Fourier transform infra-red (FTIR) spectroscopy was first employed to confirm the complete removal of organic ligands from spin coated Ni(II) 2-ethylhexanoate films, and the spectra were recorded during different time intervals upon UV light irradiation. The intensity of absorption at ≈ 1600 cm^{-1} and from 2800 cm^{-1} to 2900 cm^{-1} weakened to almost zero after 16 hours of UV irradiation (shown in **Figure S2**); these absorption features can be assigned to the C=O and C-H vibrational stretching frequencies of the organic ligands, respectively.[14c, 18] The decline of the IR vibration signals associated with the organic ligands therefore revealed the complete decomposition of 2-ethylhexanoate precursor. The 20-hour UV light irradiation was followed by annealing in air at 400 °C for 2 h to transform the deposited Ni(II) 2-ethylhexanoate into NiO_x. The decomposition process can be illustrated in the following reactions:[19]

$$[CH_3(CH_2)_3CH(C_2H_5)CO_2]_2Ni] \xrightarrow{UV\ h\nu} Ni^0 + CO_2 + \text{organic products} \quad (1)$$

$$Ni^0 \xrightarrow{air} NiO_x \quad (2)$$

Amorphous metal oxide film fabricated by PMOD has been proven to possess higher catalytic activity than crystalline films,[14c] and contain minimal carbon contamination due to the complete removal of organic ligands under UV illumination.

The morphology of the photoanode was investigated using field emission scanning electron microscopy (FESEM), and the top-view and cross-section view of the samples are shown in **Figure 2**. In the case of uncatalyzed $BiVO_4$ sample, it is clear from the surface morphology (**Figure 2a**) that it is composed of interconnected particles, with grain size ranging from ≈ 200–400 nm. This was successfully achieved by introducing PVP in the precursor as a sacrificial polymer, as reported previously.[20] The

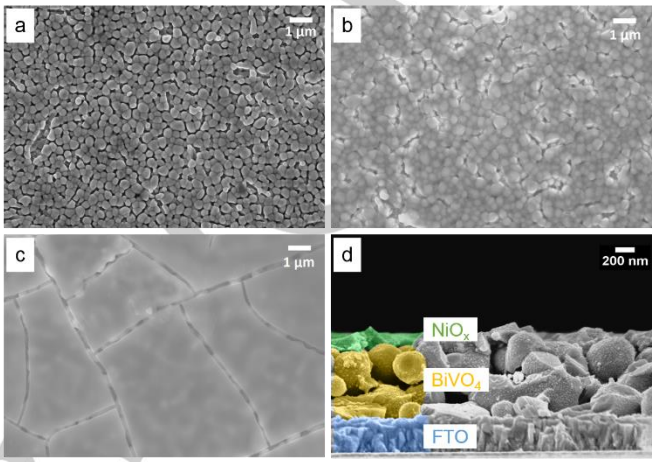

Figure 2. FESEM images of a) uncatalyzed Mo:$BiVO_4$ surface; b) NiO_x-400 °C $BiVO_4$ surface; c) NiO_x-200 °C $BiVO_4$ surface; d) NiO_x-400 °C $BiVO_4$, cross-section view. The false color indicates different layers: green for NiO_x, yellow for $BiVO_4$, and blue for FTO.

introduction of porosity increases the number of catalytic sites and light absorption in $BiVO_4$.[4, 21] The existence of the NiO_x layer on top of the NiO_x-400 °C $BiVO_4$ sample can be clearly observed in **Figure 2b**. It is observed that the NiO_x film is cracked presumably during annealing, leading to the formation of fragments, leaving a small area of $BiVO_4$ surface uncovered. Differently, NiO_x-200 °C $BiVO_4$ sample has NiO_x covered almost the whole surface **(Figure 2c)**. Based on the cross-section image **(Figure 2d)**, the thicknesses of the tri-layer Mo:$BiVO_4$ and the NiO_x layer of NiO_x-400 °C samples are estimated to be ≈ 750 nm and ≈ 150 nm, respectively.

The UV-Vis absorption spectra (**Figure S3a**) reveal that the NiO_x loading has no significant effect on the absorption profile of the $BiVO_4$ films (minor differences are due to variation in films' reflectance after NiO_x loading).The band gap of $BiVO_4$ is unaffected with the NiO_x loading (indirect band gap 2.3 eV, direct band gap 2.6 eV for all films, see **Figure S3b-d**). This band gap is consistent with a typical band gap of the monoclinic scheelite phase of $BiVO_4$, which is further confirmed by the X-ray diffraction (XRD) patterns (peaks match JCPDS no. 014-0688, **Figure 3a**). The NiO_x layers both annealed at 200 °C and 400 °C are amorphous (**Figure S4**); no additional peak is observed in the XRD patterns of catalyst loaded Mo:$BiVO_4$ **(Figure 3a)**, which is in agreement with literature results.[14c, 18]

PEC measurements and XPS analysis

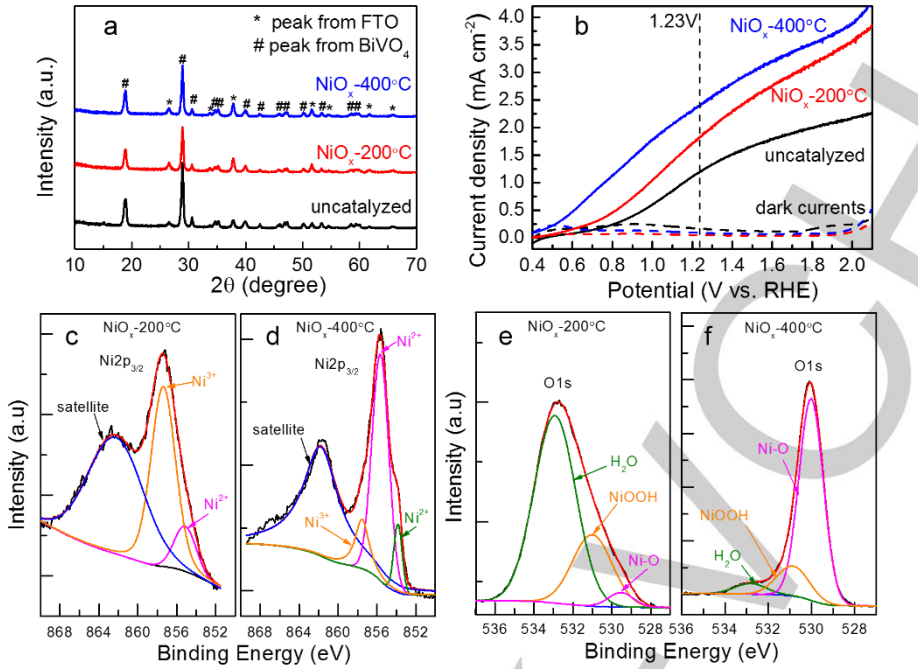

Figure 3. a) XRD patterns of the uncatalyzed and NiO_x loaded $BiVO_4$, b) Current density -potential curve of uncatalyzed and NiO_x loaded samples under light and dark conditions. High resolution XPS spectra of (c and d) Ni 2p and (e and f) O 1s of NiO_x-200 °C and NiO_x-400 °C samples.

Water oxidation performances of uncatalyzed, NiO_x-200 °C, and NiO_x-400 °C $BiVO_4$ photoanodes were evaluated in 0.5 M Na_2SO_4 (pH 6.8) solution, and the linear sweep voltammetry (LSV) under dark and illuminated conditions is shown in **Figure 3b**. Under simulated solar illumination (AM 1.5G, 100 mW cm^{-2}), the NiO_x loaded photoanodes exhibit remarkable increase of photocurrent density as compared to the uncatalyzed graded Mo:$BiVO_4$. The photocurrent density of the NiO_x-200 °C and NiO_x-400 °C samples at 1.23 V vs. RHE reach 1.9 and 2.44 mA cm^{-2}, respectively. These photocurrents represent a significant ≈ 2-fold improvement as compared to the 1.18 mA cm^{-2} photocurrent of the uncatalyzed $BiVO_4$. The different PEC performance of NiO_x-200 °C and NiO_x-400 °C could be interpreted by the different chemical compositions of each NiO_x layers, as further described below.

The chemical compositions of uncatalyzed and NiO_x/Mo:$BiVO_4$ samples were analyzed using X-ray photoelectron Spectroscopy (XPS). All expected elements (Bi, V, O, Ni and adventitious carbon) are observed, and there is no evidence for contamination of other species (**Figure S5**). The fitted Bi $4f_{7/2}$ and V $2p_{3/2}$ peaks correspond to binding energies at ≈ 159.08 eV and ≈ 516.70 eV, respectively. The Bi 4f peak at 159.08 eV is characteristic of Bi^{3+} oxidation state while the V 2p binding energy can be assigned to the oxidation state of V^{5+}.[22] No Mo peak is observed in the survey spectra as well as in the high resolution peak since the top layer consists of only undoped $BiVO_4$ and the concentration of Mo in our films is at the edge of the resolution of XPS (see **Figure 1**). Moreover, in the case of NiO_x-200 °C sample, the Bi and V peaks are highly attenuated due to the near-complete coverage of NiO_x layer (see from **Figure 2c**).

To have a better understanding on the catalytic effect of the NiO_x species, it is essential to identify the oxidation states of Ni. High resolution XPS Ni 2p spectra of both NiO_x-200 °C and NiO_x-400 °C samples are deconvoluted into different components as shown in **Figure 3c and d**. In both cases, the Ni $2p_{3/2}$ peaks are located at ≈ 852 – 868 eV with a main peak and a satellite peak (≈ 862 eV).[23] The Ni $2p_{3/2}$ main peak is deconvoluted to three peaks. The peak appeared at ≈ 857.3 eV is due to the presence of Ni^{3+} states and the peak at ≈ 855 eV corresponds to NiO.[8b, 23-24] In the case of NiO_x-400 °C an additional small peak at ≈ 854 eV is observed, which is also responsible for the Ni-O bonding in NiO.[23a, 25] The presence of NiOOH has been reported to be caused from the in-situ transformation of surface NiO.[8b] The high resolution O1s spectra (**Figure 3e and f**) corroborates with this explanation. For both, we observed oxygen peak due to surface adsorbed H_2O (≈ 533 eV),[26] hydroxyl oxygen from NiOOH (≈ 532 eV)[27] and oxygen corresponding to Ni-O bonds (≈ 529 eV).[8b, 23a] Higher NiO content is clearly observed in NiO_x-400 °C; the ratio of Ni^{2+} (i.e., NiO) to the total Ni content is calculated to be 84% in the NiO_x-400 °C sample and only 18% in the NiO_x-200 °C sample. In other words, NiOOH is the dominant phase in the NiO_x-200 °C sample and only traces of NiOOH is found in the NiO_x-400 °C sample (**Figure 3c and d**). This is also consistent with the higher surface adsorbed H_2O intensity for the NiO_x-200 °C sample, as a self-discharge reaction of the NiOOH ($2NiOOH + H_2O \rightarrow 2\ Ni(OH)_2 + 1/2\ O_2$) has been reported to occur.[28]

The different annealing temperatures therefore clearly result in two different samples with distinct compositions (NiOOH and NiO). Although a Ni^{2+}/Ni^{3+} redox system is present in both cases for facilitating better catalytic water oxidation, the content of NiO in NiO_x-400 °C is much higher than that in NiO_x-200 °C sample. This possibly indicates that NiO has superior catalytic ability and/or better suppresses surface recombination on our $BiVO_4$ than NiOOH. More detailed identification of this requires further studies, which is beyond the scope of this paper. Since the NiO_x-400 °C sample has the highest performance, from here onwards we restrict our discussion to this sample in comparison to the uncatalyzed sample (graded Mo:$BiVO_4$).

Apart from the photocurrent density increase, a cathodic shift in the onset potential for water oxidation current is also observed for the catalyst modified photoanodes (**Figure 4a**). The onset potential is cathodically shifted ≈ 70 mV to 0.35 V vs. RHE for the NiO_x-400 °C sample in comparison with the uncatalyzed one (0.42 V vs. RHE), further supporting the ability of NiO_x to reduce surface recombination.[5] The stability of the uncatalyzed and NiO_x-400 °C samples was tested in 0.5 M Na_2SO_4 under simulated sunlight and applied potential of 1.23 V vs. RHE. The photocurrent densities of both samples remain stable up to 1000 s (**Figure 4b**). Despite some fluctuations (possibly due to bubbles accumulation), the photocurrent of the NiO_x-400 °C sample recovers to the initial level, showing no degradation of stability within 9000 s (2.5 h) (**Figure S6**). In contrast, the photocurrent of the uncatalyzed sample is degraded by ≈ 30 % during this time-scale.

Incident photon-to-current conversion efficiencies (IPCE) measurements were carried out as shown in **Figure 4c**. The IPCE of NiO_x-400 °C correspond well with its enhanced water oxidation performance. The IPCE reaches a value of 53 % at wavelength of 360 nm (at 1.23 V vs. RHE), while that of uncatalyzed sample is only 20 %. All the samples absorb visible light up to ≈ 540 nm, consistent with the bandgap of 2.3 eV. The photocurrent density integrated from IPCE spectra matches well with PEC measurement values (1.1 mA cm^{-2} for uncatalyzed film, 2.4 mA cm^{-2} for NiO_x-400 °C) by equation 3:

$$J = \frac{\int_{\lambda 1}^{\lambda 2} \lambda \, \mathrm{IPCE}(\lambda) E(\lambda) d\lambda}{1240} \qquad (3)$$

where λ_1 and λ_2 define the integration wavelength range, IPCE(λ) is the measured IPCE value as a function of wavelength λ at 1.23 V vs. RHE and E(λ) is the solar spectral irradiance at one specific wavelength λ.

Role of NiO_x on $BiVO_4$

To examine the effect of NiO_x on the bulk charge separation and surface charge transfer of $BiVO_4$, photoelectrochemical measurements were carried out in Na_2SO_4 electrolyte containing Na_2SO_3 as hole scavenger (definition and calculation steps described in the Supporting Information). With hole scavenger, the photocurrent density of the NiO_x-400 °C sample is increased sharply (a factor of ≈ 2) at potentials below 1.3 V vs. RHE (**Figure S7**). A photocurrent of ≈ 4.2 mA cm^{-2} is achieved for the NiO_x-400 °C sample at 1.23 V vs. RHE, which is 56 % of the theoretical photocurrent (7.5 mA cm^{-2}) that can be achieved by $BiVO_4$. The charge transfer efficiency (η_{trans}) of this sample is overall higher than that of uncatalyzed, indicating the ability of NiO_x to suppress recombination on $BiVO_4$ surface and/or enhanced catalytic activity for OER (**Figure 4d)**. Surprisingly, the charge separation efficiency (η_{sep}) increases considerably with NiO_x deposition, and this increase is even higher at more positive potentials (**Figure 4e**). At 1.23 V vs. RHE, η_{sep} of the NiO_x-400 °C sample is more than twice that of the uncatalyzed sample, which vividly shows improvement in charge separation due to NiO_x loading. This is particularly interesting since NiO_x layer, which is a surface modification layer on the $BiVO_4$, is typically not expected to affect transport of carriers to the surface. Our observation therefore clearly shows that NiOx truly has multi-functionality when deposited on our $BiVO_4$ photoanodes.

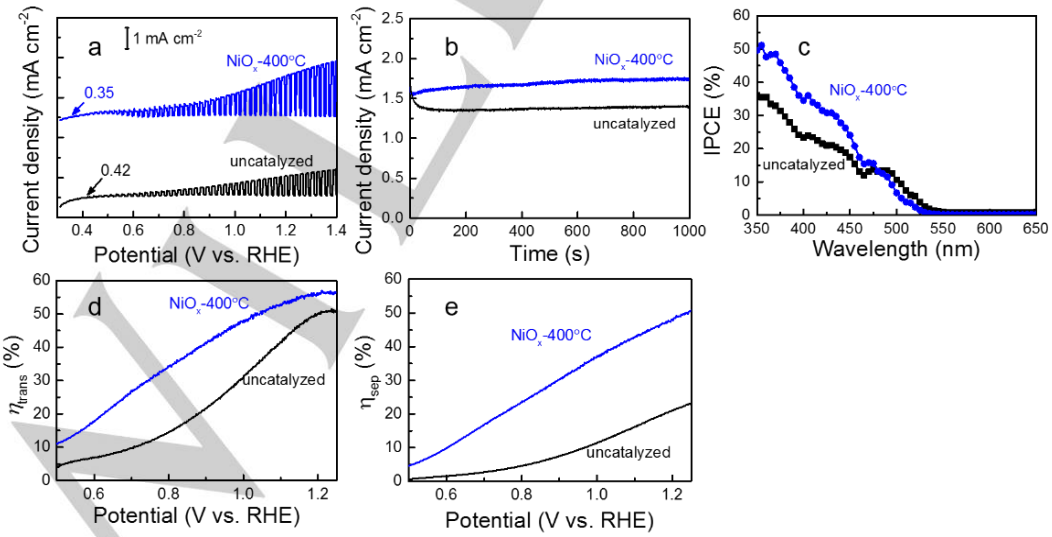

Figure 4. a) Comparison of onset potential under chopped illumination, showing cathodic shift after catalyst loading. b) Stability test for 1000 s. c) IPCE of uncatalyzed and NiO_x-400 °C $BiVO_4$ samples at 1.23V vs. RHE. Calculated d) charge transfer efficiency and e) charge separation efficiency in the potential range 0.5 V to 1.3 V vs. RHE. All measurements shown are done under AM 1.5G illumination (100 mW cm^{-2}) in 0.5 M Na_2SO_4 electrolyte (pH 6.8).

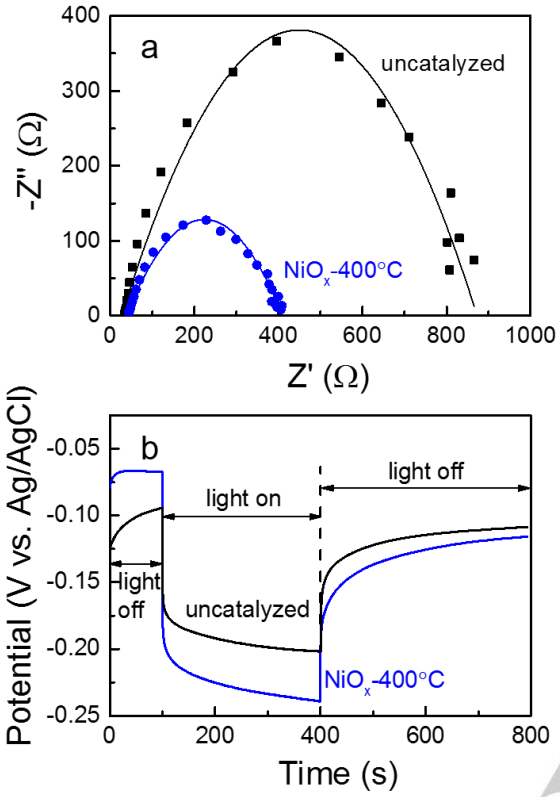

Figure 5. a) Nyquist plots of uncatalyzed and NiO_x-400 °C $BiVO_4$ measured in 0.5 M Na_2SO_4 at 1.23 V vs. RHE under AM1.5 illumination. b) Open circuit potential measurements in 0.5 M Na_2SO_4; The light turns on at 100 s and turns off at 400 s.

The charge transfer efficiency at the electrode/electrolyte interface was further analyzed by electrochemical impedance spectroscopy (EIS). **Figure 5a** shows the Nyquist plot of the uncatalyzed and NiO_x-400 °C samples under simulated solar light at 1.23 V vs. RHE in 0.5 M Na_2SO_4. The radius of the semicircle is clearly decreased upon NiO_x loading. This parameter is typically assigned to the charge transfer resistance at the electrode/electrolyte interface; lower charge transfer resistance of the NiO_x-400 °C sample is in agreement with the better charge transfer efficiency observed in **Figure 4d** due to catalyst modification.

We now turn our attention to the enhanced separation efficiency due to NiO_x modification. A possible explanation for this is that NiO_x forms a solid-solid junction on the surface of $BiVO_4$, thereby modifying the band bending (i.e., extend of the space charge region). An enlarged band banding implies higher number of holes arriving at the interface, i.e., a higher η_{sep}.[8b, 13b] This is supported by the significantly higher hole scavenger photocurrent of the NiO_x-400 °C sample as compared to the uncatalyzed sample (**Figure S6**). In the presence of hole scavenger, the surface loss mechanisms are typically assumed to be negligible; enhanced photocurrent therefore indicates more efficient hole arrival to the surface. To test this argument further, we performed open circuit potential (OCP) measurements under dark and illumination, as a simple method to obtain qualitative information about the Fermi level and band bending.[29] OCP measurements were conducted in 0.5 M Na_2SO_4 in dark and AM 1.5 G illuminated conditions for uncatalyzed and NiO_x-400 °C photoanodes. The open circuit potential difference between dark and light voltages directly reflects the extent of band bending in both samples. The OCP measured before and after illumination is shown in **Figure 5b** and it is evident that the NiO_x-400 °C sample has an enlarged ΔOCP value as compared to the uncatalyzed sample (≈ 200 mV vs. ≈ 100 mV). This is very well in agreement with the explanation above, and further supports the already observed enhanced separation efficiency. Interestingly, we note that the difference of ΔOCP value between the NiO_x-400 °C and the uncatalyzed sample (≈ 100 mV) is in very well agreement with the observed cathodic shift in the photocurrent onset potential (≈ 70 mV, see **Figure 4a**), suggesting that this cathodic shift may be a result of higher generated photovoltage.[30]

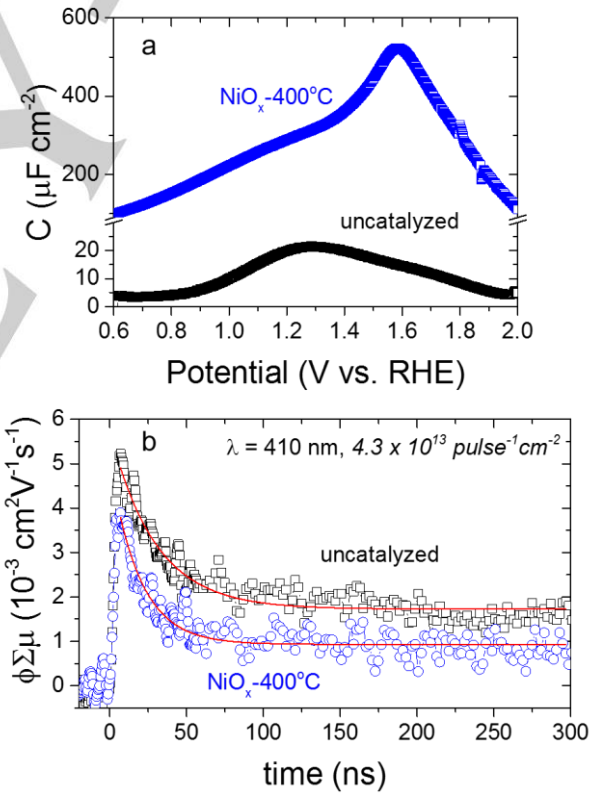

Figure 6. a) Baseline-corrected capacitance vs. potential curves of uncatalyzed and NiO_x-400 °C $BiVO_4$, obtained from rapid scan voltammetry (RSV) performed at 1 V s^{-1} in dark. RSV curves are shown in **Figure S9**. b) TRMC signal (fSm) as a function of time for uncatalyzed and NiO_x-400 °C samples. Carrier mobility can be obtained from the peak of the curve, and carrier lifetime can be obtained by fitting the curve with an exponential decay function. The solid red lines are the fit for each curve, resulting in a carrier lifetime value of 29.6 ± 1.4 ns for the uncatalyzed sample and 19.2 ± 1.0 ns for the NiO_x-400 °C sample.

To further reveal the role of NiO_x on our $BiVO_4$ films, we performed rapid scan voltammetry (RSV) measurements. Here, the samples were conditioned at a positive potential of 2.1 V vs. RHE for 2 minutes, and followed by a rapid (1 V s^{-1}) negative sweep of potential. By comparing the current-voltage curves, with and without conditioning (**Figure S9**), the surface capacitance indicating hole accumulation can be determined. **Figure 6a** shows that the presence of NiO_x on the surface of $BiVO_4$ increases the capacitance by more than one order of magnitude, i.e., the amount of holes being accumulated on the surface is significantly increased. This may be caused by efficient transfer of holes from the $BiVO_4$ to the NiO_x layer, where holes can be stored much longer and electron-hole recombination can thus be avoided. Indeed, NiO has been used as a hole collector in solar cells.[31] To confirm this, time-resolved microwave conductivity (TRMC) measurements were performed. Since carriers in NiO_x are immobile, they cannot be detected with TRMC; TRMC signals therefore only correspond to the charge carriers in $BiVO_4$. A more efficient transfer of holes from $BiVO_4$ to NiO_x would be depicted by decreased carrier mobility and/or lifetime. **Figure 6b** shows that the uncatalyzed $BiVO_4$ possess a carrier mobility of 5 × 10^{-3} cm^2 V^{-1} s^{-1} and a carrier lifetime of 29.6 ± 1.4 ns. These values are smaller than the reported pristine undoped $BiVO_4$ film (4 × 10^{-2} cm^2 V^{-1} s^{-1} and 40 ns, respectively) due to Mo doping in our film.[32] Upon NiO_x loading, the carrier mobility slightly decreases to 4 × 10^{-3} cm^2 V^{-1} s^{-1} and the carrier lifetime is shortened to 19.2 ± 1.0 ns. This supports the role of NiO_x in promoting efficient charge transfer and avoiding electron-hole recombination at the surface of $BiVO_4$.

Conclusions

In summary, we showed the multifunctional role of amorphous nickel oxide when deposited as a catalyst on graded Mo doped $BiVO_4$. The modified photoanode is shown to be stable and efficient for water oxidation, generating an AM1.5G photocurrent density of 2.44 mA cm^{-2} at 1.23 V vs. RHE, which is a ≈ 2-fold improvement as compared to the uncatalyzed film. The improved performance is attributed to both enhanced bulk charge separation efficiency and more efficient surface charge transfer upon deposition of the NiO_x layer. The enhanced charge separation is caused by the modification of band bending at the surface of $BiVO_4$, as supported by the higher hole scavenger photocurrent and enlarged open circuit potential for the NiO_x-modified $BiVO_4$. The role of NiO_x in promoting efficient charge transfer is further confirmed with the combination of RSV and TRMC measurements. Overall, the simplicity of the deposition, both for the graded Mo:$BiVO_4$ film as well as the PMOD of NiO_x, presents an alternative route for a scalable synthesis of high performing photoelectrode for water oxidation. While shown for $BiVO_4$ here, the insights from our work may be generally applied to other photoelectrode materials and enable expedited developments of large scale and low cost solar water splitting devices.

Experimental Section

Fabrication of graded Mo:$BiVO_4$ photoanodes

A simple synthesis strategy is adopted to fabricate bismuth vanadate, as reported in our previous studies.[17a, 33] The precursor solution was prepared by mixing bismuth nitrate pentahydrate ($Bi(NO_3)_3$ $5H_2O$, 98 %, Sigma Aldrich) and vanadium acetylacetonate ($VO(C_5H_7O_2)_2$, 98 %, Sigma Aldrich) in 1:1 ratio (0.3 mmoles each). The solvent is a mixture of acetic acid (Sigma Aldrich), absolute ethanol and N,N dimethylformamide (Sigma Aldrich) taken in 1:1.25:1.25 ratio, respectively. 400 mg polyvinyl pyrrolidone (PVP, MW-130000, Sigma Aldrich) was then added into 3.5 mL of the precursor solution, which was further magnetically stirred at room temperature for 30 min to form a homogenous viscous solution. Molybdenum (Mo) doping was further achieved by adding ammonium molybdate tetrahydrate ($(NH_4)_6Mo_7O_{24}$ $4H_2O$, 99.98 % trace metal basis, Sigma Aldrich) into the precursor solution as mentioned above. The concentration of Mo doping was varied from 0 % to 2 % by adjusting the amount of ammonium molybdate tetrahydrate and vanadium acetyl acetonate, resulting a final solution containing 1:1 molar ratio of Bi/(V+Mo). The graded samples were fabricated by a layer-by-layer spin-coating method (2000 rpm, 45 s) on a 1 × 2 cm^2 cleaned FTO glass. All FTO substrates were sonicated successively in soap water, ethanol, acetone, deionized water (each step 20 min) and finally dried by nitrogen flow. The bottom layer consisted of 2 % Mo-doped $BiVO_4$, which was loaded through spin coating 60 µL precursor (containing 2 % Mo), and further annealed in air at 500 °C for 2 h with a heating rate 5° min^{-1}. Afterwards the second layer (1 % Mo-doped) was spin coated and annealed, so was the top layer (pure $BiVO_4$). The sequence of doping ratio is arranged to form a graded Mo doping.[1b] The prepared gradient Mo doped $BiVO_4$ (Mo:$BiVO_4$) samples were described as uncatalyzed $BiVO_4$ samples throughout the discussion. The schematic of the fabrication procedure is shown in **Figure S1**.

NiO_x catalyst deposition

PMOD method was employed to introduce NiO_x film on the as-prepared $BiVO_4$ samples. The method was previously demonstrated to be an effective technique to produce active transition metal based amorphous electrocatalyst for water oxidation.[14c, 18, 34] For this, PMOD precursor was prepared by dissolving 5 wt % (solution based) of Ni(II) 2-ethylhexanoate in hexane. Other concentrations have been explored, and 5 wt % was found to be an optimum concentration for maximizing performance. The Ni precursor was then spin coated over the uncatalyzed Mo:$BiVO_4$ thin film. Thereafter, the films were subjected to UV irradiation (λ = 254 nm, 15 W, Sankyo Denki) for 20 hours. To investigate the influence of annealing temperature, catalysts loaded $BiVO_4$ samples were annealed at 200 °C and 400 °C in a muffle furnace. The catalyst-loaded samples are named according to their Ni concentration and annealing temperature as follows: NiO_x-200 °C (coated with 5 wt % of Ni(II) precursor, annealed at 200 °C) and NiO_x-400 °C (5 wt % Ni(II) precursor, annealed at 400 °C).

Characterization and measurements

The decomposition of organic ligands was studied by Fourier transform infra-red (FTIR) spectroscopy using Thermo Scientific Nicolet Continum infra-red microscope, which has single/dual detectors such as MPT/A and InGaAs for near-IR/mid-IR/far-IR range detection.

The morphology of the photoanodes was studied using a field emission scanning electron microscopy (FESEM), JEOL-6340F and JEOL-7600F. The crystal structures of the samples were determined by X-ray diffraction (XRD) measurements using Shimadzu thin film X-ray

diffractometer with Cu Kα radiation. The surface elemental compositions of the samples were obtained by X-ray photoelectron spectroscopy (XPS) on a VG ESCALAB 220I-XL system equipped with a monochromatic Al Kα (1486.6 eV) source and a concentric hemispherical energy analyzer. The UV visible absorption studies were carried out using an UV−Vis−NIR spectrophotometer (PerkinElmer, Lambda 750S).

Photoelectrochemical (PEC) measurements were carried out using CHI 660D working station (CH Instruments, Inc.) in combination with a 150 W xenon solar simulator (67005, Newport Corp.) equipped with a solar filter (KG 3) to achieve the measured light intensity to AM 1.5G (100 mW cm^{-2}). A three-electrode configuration was used where the $NiO_x/BiVO_4$ samples served as the anode, a Pt coil (≈ 3.6 cm^2) as the counter electrode, Ag/AgCl (3 M KCl) as the reference electrode, and 0.5 M Na_2SO_4 (pH 6.8) as the electrolyte. The conversion between voltage vs. Ag/AgCl and reversible hydrogen electrode (RHE) is performed using the equation below:

$$E \text{ (vs. RHE)} = E \text{ (vs. Ag/AgCl)} + E^{o}_{Ag/AgCl\ (reference)} + 0.0591 \times pH \quad (4)$$

where $E^{o}_{Ag/AgCl(reference)} = 0.21$ vs. NHE at 298 K (5)

The effective working electrode surface area is 0.125 cm^2, determined by the PEC cell used. Prior to all PEC measurements the electrolyte was degassed with nitrogen for 15 minutes. The photocurrent responses of the samples were measured using linear sweep voltammetry (LSV) under dark and illuminated conditions at a scan rate of 20 mV s^{-1}. Incident photon to current conversion efficiency (IPCE) data were measured from 350 to 650 nm wavelength at 1.23 V vs. RHE, with the combination of a xenon light source (MAX-302, Asahi Spectra Co. Ltd.) and a monochromator (CMS-100, Asahi Spectra Co. Ltd.). The intensity of the monochromatic light was determined by measuring the photocurrent of a calibrated Si photodiode (Bentham, DH-Si) using a source meter (Keithley Instruments Inc., model No. 2400). At each specific wavelength, the IPCE is calculated using the equation 6.

$$\text{IPCE}(\%) = \frac{1240\ (\text{V nm}) \times \text{Photocurrent density (mA cm}^{-2})}{\text{Incident light power density (mW cm}^{-2}) \times \text{Wavelength (nm)}} \quad (6)$$

To study the charge transfer efficiency of the photoanodes, electrochemical impedance spectroscopy (EIS) measurements under illuminated conditions were performed using an automated potentiostat (Metrohm-Autolab, AUT 83285) in a three-electrode configuration. The reference and counter electrodes were the same as those used in PEC measurements. Rapid scan voltammetry measurements were performed by applying a constant potential of 2.1 V vs. RHE for 2 mins, followed by a quick potential sweep to 0.6 V vs. RHE with a scan rate of 1 V s^{-1}.

Time-resolved microwave conductivity (TRMC) measurements were carried out in a cavity cell using a wavelength tunable 50 Hz Nd:YAG laser with a 3 ns pulse. The wavelength of excitation used in this study was 410 nm. A voltage controlled oscillator (Sivers IMA VO3262X) was applied to generate microwaves in the X-band region (8.4–8.7 GHz). The dielectric constant of $BiVO_4$ was taken as 68.[35] More detailed description of the TRMC measurement can be found in previous reports.[32, 36]

Acknowledgements

The authors would like to thank financial support from the Singapore Ministry of Education (MOE) Tier 2 grant (MOE2016T21030). This work was partially funded by the German Federal Ministry of Education and Research (BMBF), Singapore-German project “CT-PEC” (01DP14011).

Conflict of interest

The authors declare no conflict of interest.

Keywords: band bending • bismuth vanadate • electrocatalyst • charge transfer • water splitting

[1] a) F. E. Osterloh, *Chem. Soc. Rev.* **2013**, *42*, 2294-2320; b) F. F. Abdi, L. Han, A. H. M. Smets, M. Zeman, B. Dam, R. van de Krol, *Nat. Commun.* **2013**, *4*, 2195
[2] a) J. A. Seabold, K.-S. Choi, *J. Am. Chem. Soc.* **2012**, *134*, 2186-2192; b) M. F. Lichterman, M. R. Shaner, S. G. Handler, B. S. Brunschwig, H. B. Gray, N. S. Lewis, J. M. Spurgeon, *J. Phys. Chem. Lett.* **2013**, *4*, 4188-4191.
[3] F. F. Abdi, R. van de Krol, *J. Phys. Chem. C* **2012**, *116*, 9398-9404.
[4] Y. Park, K. J. McDonald, K.-S. Choi, *Chem. Soc. Rev.* **2013**, *42*, 2321-2337.
[5] J. Su, L. Guo, N. Bao, C. A. Grimes, *Nano Lett.* **2011**, *11*, 1928-1933.
[6] D. Eisenberg, H. S. Ahn, A. J. Bard, *J. Am. Chem. Soc.* **2014**, *136*, 14011-14014.
[7] a) Y. Park, D. Kang, K.-S. Choi, *Phys. Chem. Chem. Phys.* **2014**, *16*, 1238-1246; b) J. A. Seabold, K. Zhu, N. R. Neale, *Phys. Chem. Chem. Phys.* **2014**, *16*, 1121-1131; c) K. Ding, B. Chen, Z. Fang, Y. Zhang, Z. Chen, *Phys. Chem. Chem. Phys.* **2014**, *16*, 13465-13476.
[8] a) T. W. Kim, K.-S. Choi, *Science* **2014**, *343*, 990-994; b) M. Zhong, T. Hisatomi, Y. Kuang, J. Zhao, M. Liu, A. Iwase, Q. Jia, H. Nishiyama, T. Minegishi, M. Nakabayashi, N. Shibata, R. Niishiro, C. Katayama, H. Shibano, M. Katayama, A. Kudo, T. Yamada, K. Domen, *J. Am. Chem. Soc.* **2015**, *137*, 5053-5060; c) X. Chang, T. Wang, P. Zhang, J. Zhang, A. Li, J. Gong, *J. Am. Chem. Soc.* **2015**, *137*, 8356-8359.
[9] Y. Liang, J. Messinger, *Phys. Chem. Chem. Phys.* **2014**, *16*, 12014-12020.
[10] Y. Pihosh, I. Turkevych, K. Mawatari, J. Uemura, Y. Kazoe, S. Kosar, K. Makita, T. Sugaya, T. Matsui, D. Fujita, M. Tosa, M. Kondo, T. Kitamori, *Sci. Rep.* **2015**, *5*, 11141.
[11] Y. Liu, Y. Guo, L. T. Schelhas, M. Li, J. W. Ager, *J. Phys. Chem. C* **2016**, *120*, 23449-23457.
[12] a) D. K. Zhong, S. Choi, D. R. Gamelin, *J J. Am. Chem. Soc.* **2011**, *133*, 18370-18377; b) C. Zachäus, F. F. Abdi, L. M. Peter, R. van de Krol, *Chem. Sci.* **2017**, *8*, 3712-3719.
[13] a) M. R. da Silva, L. V. A. Scalvi, V. S. L. Neto, L. H. Dall'Antonia, *J. Mater. Sci. Mater. Electron.* **2015**, *26*, 7705-7714; b) S. Xie, T. Zhai, Y. Zhu, W. Li, R. Qiu, Y. Tong, X. Lu, *Int. J. Hydrogen Energy* **2014**, *39*, 4820-4827.
[14] a) Y. Jiao, Y. Zheng, M. Jaroniec, S. Z. Qiao, *Chem. Soc. Rev.* **2015**, *44*, 2060-2086; b) Z. W. Seh, J. Kibsgaard, C. F. Dickens, I. Chorkendorff, J. K. Nørskov, T. F. Jaramillo, *Science* **2017**, *355*, 6321; c) R. D. L. Smith, M. S. Prévot, R. D. Fagan, Z. Zhang, P. A. Sedach, M. K. J. Siu, S. Trudel, C. P. Berlinguette, *Science* **2013**, *340*, 60-63.
[15] K. Sun, F. H. Saadi, M. F. Lichterman, W. G. Hale, H.-P. Wang, X. Zhou, N. T. Plymale, S. T. Omelchenko, J.-H. He, K. M. Papadantonakis, B. S. Brunschwig, N. S. Lewis, *Proc. Natl. Acad. Sci.* **2015**, *112*, 3612-3617.
[16] M. Zhong, T. Hisatomi, T. Minegishi, H. Nishiyama, M. Katayama, T. Yamada, K. Domen, *J. Mater. Chem. A* **2016**, *4*, 9858-9864.
[17] a) R. P. Antony, P. S. Bassi, F. F. Abdi, S. Y. Chiam, Y. Ren, J. Barber, J. S. C. Loo, L. H. Wong, *Electrochim. Acta*. **2016**, *211*, 173-182; b) R. P. Antony, M. Zhang, K. Zhou, S. C. J. Loo, J. Barber, L. H. Wong, *ACS Omega* **2018**, *3*, 2724-2734.
[18] R. D. L. Smith, M. S. Prévot, R. D. Fagan, S. Trudel, C. P. Berlinguette, *J. Am. Chem. Soc.* **2013**, *135*, 11580-11586.
[19] R. H. Hill, A. A. Avey, S. L. Blair, M. Gao, B. J. Palmer, *Mater. Chem. Phys.* **1996**, *43*, 233-237.
[20] M. Zhu, D. Meng, C. Wang, G. Diao, *ACS Appl. Mater. Interfaces* **2013**, *5*, 6030-6037.
[21] H. S. Park, K. E. Kweon, H. Ye, E. Paek, G. S. Hwang, A. J. Bard, *J. Phys. Chem. C* **2011**, *115*, 17870-17879.
[22] S. K. Pilli, T. E. Furtak, L. D. Brown, T. G. Deutsch, J. A. Turner, A. M. Herring, *Energy Environ. Sci.* **2011**, *4*, 5028-5034.
[23] a) A. N. Mansour, *Surf. Sci. Spectra* **1994**, *3*, 231-238; b) D. S. Hall, D. J. Lockwood, C. Bock, B. R. MacDougall, *Proc. Math. Phys. Eng. Sci.* **2015**, *471*, 20140792.
[24] S. Oswald, W. Brückner, *Surf. Interface Anal.* **2004**, *36*, 17-22.
[25] M. C. Biesinger, B. P. Payne, L. W. M. Lau, A. Gerson, R. S. C. Smart, *Surf. Interface Anal.* **2009**, *41*, 324-332.
[26] M. A. Peck, M. A. Langell, *Chem. Mater.* **2012**, *24*, 4483-4490.

[27] E. L. Ratcliff, J. Meyer, K. X. Steirer, A. Garcia, J. J. Berry, D. S. Ginley, D. C. Olson, A. Kahn, N. R. Armstrong, *Chem. Mater.* **2011**, *23*, 4988-5000.
[28] Z. Mao, R. E. White, *J. Electrochem. Soc.* **1992**, *139*, 1282-1289.
[29] a) J. C. Blakesley, N. C. Greenham, *J. Appl. Phys.* **2009**, *106*, 034507; b) J. Bisquert, A. Zaban, M. Greenshtein, I. Mora-Seró, *J. Am. Chem. Soc.* **2004**, *126*, 13550-13559.
[30] C. Du, X. Yang, M. T. Mayer, H. Hoyt, J. Xie, G. McMahon, G. Bischoping, D. Wang, *Angew. Chem. Int. Ed.* **2013**, *52*, 12692-12695.
[31] a) J. Bandara, H. Weerasinghe, *Sol. Energy Mater. Sol. Cells* **2005**, *85*, 385-390; b) Z. Liu, M. Zhang, X. Xu, F. Cai, H. Yuan, L. Bu, W. Li, A. Zhu, Z. Zhao, M. Wang, Y.-B. Cheng, H. He, *J. Mater. Chem. A* **2015**, *3*, 24121-24127.
[32] F. F. Abdi, T. J. Savenije, M. M. May, B. Dam, R. van de Krol, *J. Phys. Chem. Lett.* **2013**, *4*, 2752-2757.
[33] W. Luo, Z. Yang, Z. Li, J. Zhang, J. Liu, Z. Zhao, Z. Wang, S. Yan, T. Yu, Z. Zou, *Energy Environ. Sci.* **2011**, *4*, 4046-4051.
[34] S. Trudel, E. Daryl Crozier, R. A. Gordon, P. S. Budnik, R. H. Hill, *J. Solid State Chem.* **2011**, *184*, 1025-1035.
[35] D. Zhou, L.-X. Pang, J. Guo, Z.-M. Qi, T. Shao, Q.-P. Wang, H.-D. Xie, X. Yao, C. A. Randall, *Inorg. Chem.* **2014**, *53*, 1048-1055.
[36] a) M. Ziwritsch, S. Müller, H. Hempel, T. Unold, F. F. Abdi, R. van de Krol, D. Friedrich, R. Eichberger, *ACS Energy Lett.* **2016**, *1*, 888-894; b) F. F. Abdi, A. Chemseddine, S. P. Berglund, R. van de Krol, *J. Phys. Chem. C* **2017**, *121*, 153-160.

Entry for the Table of Contents (Please choose one layout)

Layout 1:

FULL PAPER

Nickel oxide (NiO_x) loading on $BiVO_4$ photoanode demonstrates a 2-fold improvement of photocurrent density as compared with the uncatalyzed one. NiO_x modification increases both the charge separation and the charge transfer efficiency significantly, which attributes to larger band bending and promoted charge transfer at the surface of $BiVO_4$.

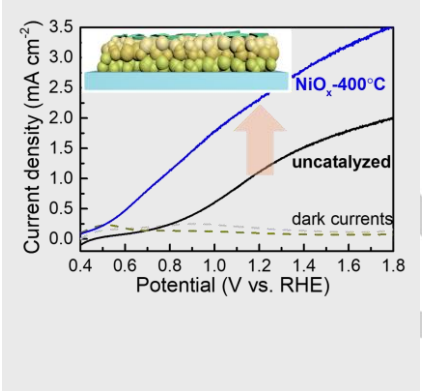

Mengyuan Zhang, Rajini P. Antony, Sing Yang Chiam, Fatwa Firdaus Abdi, Lydia Helena Wong**

Page No. – Page No.

Understanding the Roles of NiO_x in Enhancing the Photoelectrochemical Performance of $BiVO_4$ Photoanodes for Solar Water Splitting